



Fabrication, bacteriostasis and osteointegration properties researches of the additively-manufactured porous tantalum scaffolds loading vancomycin

Hu Qian^{a,c,d,1}, Ting Lei^{a,1}, Long Hua^a, Yu Zhang^a, Dongyu Wang^a, Jiangyu Nan^a, Wenbin Liu^a, Yan Sun^a, Yihe Hu^{a,b,*}, Pengfei Lei^{a,b,**}

^a Department of Orthopedic Surgery, Xiangya Hospital Central South University, Changsha, 410008, China

^b Department of Orthopedic Surgery, The First Affiliated Hospital, College of Medicine, Zhejiang University, China

^c Department of Orthopaedic Surgery, Affiliated Hospital of Zunyi Medical University, Zunyi, China

^d Xiangya School of Medicine, Central South University, Changsha, 410008, China

ARTICLE INFO

Keywords:

Infected bone defects
Porous tantalum
PLGA microspheres
Vancomycin

ABSTRACT

Infected bone defects (IBDs) remains a challenging problem for orthopedists. Clinically, routine management for IBDs has two stages: debridement and systematic antibiotics administration to control infection, and secondary grafting to repair bone defects. Whereas the efficacy is not satisfactory, because the overuse of antibiotics may lead to systemic toxicity, and the emergence of drug-resistant bacteria, as well as the secondary surgery would cause additional trauma and economic burden to the patients. Therefore, it is imperative to develop a novel scaffold for one-stage repair of IBDs. In this study, vancomycin (Van) was encapsulated into poly(lactic co-glycolic acid) (PLGA) microspheres through the double emulsion method, which were then loaded into the additively-manufactured porous tantalum (AM-Ta) through gelatin methacryloyl (GelMA) hydrogel to produce the composite Ta/GelMA hydrogel (Gel)/PLGA/vancomycin(Van) scaffolds for repairing IBDs. Physicochemical characterization of the newly-developed scaffold indicated that the releasing duration of Van was over 2 weeks. Biological experiments indicated good biocompatibility of the composite scaffold, as well as bacteriostasis and osteointegration properties, which showed great potential for clinical application. The construction of this novel scaffold would provide new sight into the development of orthopaedic implants, shedding a novel light on the treatment of IBDs.

1. Introduction

According to the statistics, about 20 million patients around the world lose bone tissue due to various diseases every year [1]. Especially, treatment of infected bone defects (IBDs) appeared as an arduous challenge for orthopedists [2]. Currently, the routine management for IBDs contained thorough debridement, administration of high-dose antibiotics to control infection, followed by implantation of grafts to repair bone defects. However, either insufficient or excessive debridement would lead to serious consequences. The overuse of high-dose antibiotics may not only bring about systemic toxicity, but also contribute to the emergence of drug-resistant bacteria [3]. Since Buchholz et al. proposed to add antibiotics into polymethyl methacrylate (PMMA) to

address infection around orthopaedic implants for the first time in the 1970s, antibiotics-loaded PMMA has been widely used clinically [4]. While this method still has some unavoidable disadvantages. Firstly, PMMA is not biodegradable and needs to be replaced through the second-stage operation, causing additional trauma and economic burden to the patients [5]. Secondly, the releasing efficiency of antibiotics from PMMA is unsatisfactory, which impedes the removal of local pathogens [6]. The main difficulties in dealing with IBDs are the elimination of pathogenic bacteria and structural reconstruction of bone defects. Therefore, it makes profound sense to fabricate novel scaffolds with sufficient mechanical strength and long-acting antibacterial efficiency to repair infected bone defects at one stage [7].

Tantalum (Ta) metal has been widely used in orthopaedic surgeries

Peer review under responsibility of KeAi Communications Co., Ltd.

* Corresponding author. Department of Orthopedic Surgery, Xiangya Hospital Central South University, Changsha, 410008, China.

** Corresponding author. Department of Orthopedic Surgery, Xiangya Hospital Central South University, Changsha, 410008, China.

E-mail addresses: xy_huyh@163.com (Y. Hu), leipengfei@zju.edu.cn (P. Lei).

¹ These authors contributed equally to this work: Hu Qian: moneylakecsu@163.com, Ting Lei: leiting19950415@gmail.com

<https://doi.org/10.1016/j.bioactmat.2022.12.013>

Received 27 August 2022; Received in revised form 1 November 2022; Accepted 16 December 2022

2452-199X/© 2023 The Authors. Published by KeAi Communications Co., Ltd. This is an open access article under the CC BY-NC-ND license (<http://creativecommons.org/licenses/by-nc-nd/4.0/>).

due to its good biocompatibility, corrosion resistance and osteointegration property, which has attracted increasing attention over the past decades [8]. In particular, since the emergence of Trabecular Metal™ (TM), a commercial porous Ta product prepared by Zimmer (USA) using chemical vapor deposition, the application of porous Ta had extended explosively [9]. However, high melting point and affinity to oxygen make the preparation of porous Ta difficult. Meanwhile, porous Ta scaffolds prepared using traditional methods were not only expensive, but also criticized for irregular pore structure and inability to realize personalization [10]. Additive manufacturing (AM) is able to achieve personalized customization of scaffolds, and also additively-manufactured scaffolds have uniform pore structure and adjustable mechanical properties.

Poly (lactic acid-co-glycolic acid) (PLGA) is a type of biodegradable organic compound with good biodegradability, biocompatibility, film-forming and spherization properties. PLGA has become one of the most widely used drug-delivering vectors [11], which can be applied to deliver proteins, peptides, bacteria, viral DNA and various anticancer drugs [11]. At present, more than 20 PLGA-based biodegradable microspheres have been approved by the FDA, and many others are in development or clinical trials [11]. Therefore, encapsulating antibiotic with PLGA to prepare Van-loaded PLGA microspheres is a feasible and efficient approach to prolong the releasing duration.

While, it remains difficult to efficiently load the Van-encapsulated PLGA microspheres into the porous Ta scaffolds. Gelatin methacrylate (GelMA) is a bio-hydrogel material with excellent biocompatibility. Under ultraviolet light, its aqueous solution can be gelatinized into hydrogel with 3D structure, which has been widely used in bio-printing and 3D culturing of cells [12]. In addition, the latest study reported that GelMA hydrogel enhanced the osteogenic activity of Ti6Al4V [13]. In specific tissue engineering, the mechanical strength and degradation feature of GelMA hydrogel can be optimized via adjusting the concentration, composition ratio and gelatinization degree to meet various requirements [14]. As such, the GelMA hydrogel is an ideal medium for loading Van-encapsulated PLGA microspheres into porous Ta scaffolds.

In the present study, laser additive manufacturing technology was applied to prepare porous Ta scaffolds. And the Van-loaded PLGA microspheres were equipped into the porous Ta through GelMA hydrogel to construct the composite Ta/Gel/PLGA/Van scaffold for repairing IBDs. In this composite scaffold, additively-manufactured porous Ta could reconstruct the defects structurally, while the sustain-released Van could eliminate the bacteria (**Graphical abstract**). The newly-developed scaffolds showed potent potential for clinical translation and application. The present study would provide new idea for the treatment of IBDs.

2. Materials and methods

2.1. Fabrication and characterization of the composite scaffolds

2.1.1. Preparation of the Ta/Gel/PLGA/van composite scaffolds

Van-encapsulated PLGA microspheres were fabricated through the double emulsion method. Briefly, 250 mg PLGA (MACKLIN, China) was dissolved in 4.5 mL dichloromethane (Sinopharm Chemical Reagent Co., Ltd, China) through sonication, which was prepared as oil (O) phase. 100 mg vancomycin (Yeasen, China) was dissolved in 0.5 mL ddH₂O as water phase 1 (W₁). Meanwhile, 600 mg polyvinyl alcohol (PVA) (Sigma, USA) was dissolved in 20 mL ddH₂O via high-temperature heating as water phase 2 (W₂). The W₁ phase was added into the O phase to form oil-water mixture (W₁/O), which was treated with sonication of 80w for 30s repeatedly for three times. Then the pre-treated W₁/O emulsion was dripped into the PVA solution to form complex emulsion (W₁/O/W₂). After the dichloromethanes was volatiled, the prepared PLGA microspheres were cleaned with ddH₂O and centrifugated, followed by freeze drying. GelMA (Hebei Dazhou Co., Ltd., China) was dissolved in ddH₂O at 56 °C, then mixed with the Van-loaded

PLGA microspheres. GelMA solutions with different concentrations (5%, 7.5%, 10%) was produced to receive UV lighting more than 2 min for screening out appropriate GelMA concentration. And the 7.5% GelMA concentration receiving 10 s UV lighting was adopted for subsequent experiments. The porous Ta scaffolds (Zhuzhou Print Additive Manufacturing Co., Ltd., China) were immersed in the hydrogel/microsphere mixture, and ultraviolet light was applied to gelatinize the hydrogel.

2.1.2. SEM observation, EDS detection and particle size measuring

Van-encapsulated PLGA microspheres were spread out in ddH₂O firstly. After dehydration and gold spraying, the observation was performed using scanning electron microscope (SEM) (Quanta-200, FEI, Netherlands). Similarly, after the composite scaffolds were observed, representative fields were chosen for elements detection via Energy Dispersive Spectrometer (EDS). Three SEM image were selected randomly to calculate the mean particle size.

2.1.3. Drug-loading rate, encapsulation efficiency and releasing feature

Firstly, gradient vancomycin solutions were detected to produce the concentration standard curve. The Van-loaded PLGA microspheres were dissolved in dichloromethane and ddH₂O. The supernatant was collected to measure the peak value via UV spectrophotometer (UV-2450, Shimadzu, Japan), calculating the drug-loading rate and encapsulation efficiency according to the following formula:

$$\text{Encapsulation efficiency} = \frac{\text{Mass of Van in the PLGA microspheres}}{\text{Mass of the dissolved vancomycin}} \times 100\%$$

$$\text{Drug - loading rate} = \frac{\text{Mass of Van in the PLGA microspheres}}{\text{Mass of the Van - loaded PLGA microspheres}} \times 100\%$$

Regarding the releasing features of Vancomycin, at each time points, releasing liquid were extracted for detection and isometric PBS were supplemented. Additionally, porous Ta was directly immersed in Van solution for physical absorption and the releasing feature of absorbed Van was measured.

2.2. Isolation and identification of bone marrow mesenchymal stem cells (BMSCs)

2.2.1. BMSCs isolation

BMSCs were extracted by the method reported previously [15]. After sacrificing, the bilateral femur and tibia were acquired. The epiphyseal plates were removed and bone marrow was rinsed thoroughly using Dulbecco's Modified Eagle Medium: F-12 (DMEM/F-12) (Procell, China). The medium was semi-quantitatively replaced 24h later, and fully replaced 48h later.

2.2.2. Three-line differentiation

In osteogenic differentiation, BMSCs were seeded in 48-well plates as 2×10^4 /well, and the medium was replaced with osteogenic induction medium (Minimum Essential Medium α +10% fetal bovine serum (FBS) + 0.1% dual antibiotics +0.1 $\mu\text{mol/L}$ dexamethasone +50 $\mu\text{mol/L}$ ascorbic acid +10 mmol/L β -glycerol phosphate) (Cyagen, China) at 48h. After culturing for 14 days, BMSCs were stained with alizarin red solution (Cyagen, China) and observed (Leica, N2-DMI8, Germany). In adipogenic differentiation, BMSCs were cultured with adipogenic differentiation induction medium (10% FBS +1% glutamine +0.2% insulin +0.1% IBMX +0.1% rosiglitazone +2.5% dexamethasone) (Cyagen, China). Oil red O solution (Solarbio, China) was added to stain the lipid droplet at 21 days. As for chondroblast differentiation, BMSCs were cultured with chondrogenic induction medium (DMEM medium + 0.1 $\mu\text{mol/L}$ dexamethasone +1.25 mg/mL bovine serum albumin +1 mmol/L sodium pyruvate + ITS +10 ng/mL TGF- β +37.5 $\mu\text{g/mL}$ vitamin C + 1 ng/mL β -FGF) (Cyagen, China) for 14 days, and the cartilage balls were

sliced and stained with cartilage staining solution (Cyagen, China).

2.3. Biocompatibility evaluation

EDU/DAPI dual fluorescence labelling Isometric pre-heated 2X working liquid was added to the medium for labelling the proliferative BMSCs. After incubation for 12h, fixing the BMSCs with 4% PFA for 2h, adding 0.1% TritonX-100 (Solarbio, China) to penetrate the cellular membrane for 10 min. Then, 1X EDU buffer additive (APEXBIO, USA) and click reaction solution were added. DAPI solution (Solarbio, China) was added and incubated for 30 min at room temperature without light. Finally, the labelled BMSCs were observed and photographed under a fluorescence microscope (Leica, TCS SP8X, Germany).

FITC and DAPI labelling At the 1st and 3rd day after seeding, 4% PFA was applied for cellular fixation for 30min. 0.1% TritonX-100 solution was added to penetrate cell membrane for 10min. FITC-labelled phalloidin (Solarbio, China) solution was added to label the cytoskeleton for 30 min followed by DAPI staining for 10min.

Living/dead cell staining When cultured for 1 and 3 days, the cells were pre-treated with 1x Assay buffer solution. After removing the buffer, staining solution (Calcein-AM: Propidium Iodide: 1X Assay buffer = 1:3:1000) (Solarbio, China) was added to label the living and dead BMSCs.

SEM observation After removing the medium and fixing the cells at 4 °C overnight, drying the BMSCs naturally at room temperature, followed by spraying gold and observing with SEM.

For all the cell experiments, the concentration of all used antibiotics was 500 µg/mL.

2.4. In-vitro antibacterial evaluation

Bacteriostatic ring test 100 µL of diluted methicillin-resistant staphylococcus aureus, (MRSA, ATCC-43300) solution was dripped on the bacterial culture plates and scribbled evenly, and scaffolds were placed vertically. After incubating at 37 °C for 24h, photographing and measuring the diameter of bacteriostatic rings. As for disk diffusion test, after scribbling the bacteria, sterile paper with a diameter of 5 mm were put on the culturing plates, and 5 µL releasing solution were dripped on the paper.

SEM observation The matched glass was fixed in 24-well plates, and scaffolds were placed, with adding nothing as the negative control group and vancomycin as the positive control group. Bacterial solution was added in all groups. SEM observation was performed after dehydration with gradient alcohol, spraying gold, observing.

Living/dead bacterial staining The scaffolds were placed in confocal dishes, and diluted MRSA liquid was added. After incubation, isometric SYTO9 and PI (Maokang Biotechnology Co., Ltd., China) were mixed to stain the bacteria for 10 min at room temperature without light, followed by photographing under confocal microscope (Leica, TCS SP8X, Germany).

Bacterial counting 100 µL pre-treated MRSA solution were dripped and scribbled on the culture plates incubated overnight, followed by photographing and calculating the bacterial numbers.

2.5. In-vitro osteogenesis detection

When seeding directly, sterilized scaffolds were placed in the 48-well plates, and the third-generation BMSCs were seeded onto the scaffolds as 2×10^4 cells/cm². The medium was replaced with osteogenic induction medium at 48h and exchanged every two days. In terms of indirect culturation, the sterilized scaffolds were immersed in osteogenic induction medium for obtaining releasing liquid. BMSCs were seeded into 48-well plates as 2×10^4 cells/cm². From the third day, the medium was replaced with the releasing liquid. Meanwhile, isometric osteogenic differentiation induction medium was added to the wells for preparing new releasing liquid.

ALP staining/quantification After culturation for 3 and 7 days, to assess the early osteogenic status, the supernatant was collected for detection of ALP production using ALP kit (Nanjing Jiancheng Bioengineering Institute, China) [16]. After fixing the BMSCs with 4% PFA for 30 min, ALP staining solution (Yeasen, China) was added and incubated at 37 °C for 5 min, followed by photographing and quantifying with Image-J.

Alizarin red staining/quantification When cultured for 14 and 21 days, BMSCs were fixed with 4% PFA, alizarin red solution was applied to stain the mineral nodules for 15min. Finally, 10% (m/v) hexadecylpyridinium chloride (Sinopharm Group Chemical Reagent Co. LTD, China) was added to degrade the mineral nodules, and the degraded solution was collected for detecting OD value at 565 nm.

Sirius red staining/quantification Similarly, after fixation, Sirius red solution (Phygene, China) was used for staining the BMSCs. Then, 0.2 M sodium hydroxide solution (Sinopharm Group Chemical Reagent Co. LTD, China) was used for deposing the stained COL-I, and the degraded solution was collected for detecting OD value at 540 nm.

qRT-PCR RNA was extracted using Trizol (Yeasen, China). After detecting the concentration of RNA, reverse transcription was performed according to the instruction. Finally, qRT-PCR was conducted using the RT-qPCR SYBR Green Kit (Yeasen, China)

2.6. In-vivo efficiency in repairing bone defects

This animal experiment was approved by the Ethics Committee of Central South University, and all procedures were conducted in accordance with relevant experimental specifications strictly. Briefly, SD rats were anesthetized with 2% pentobarbital sodium intraperitoneally. After shaving, disinfection and incision, a $\Phi 3\text{mm} \times 4\text{ mm}$ cylindrical bone defect was made in the distal femur using medical electric drill, and scaffolds were implanted subsequently, followed by suturing and marking. Alizarin red (30 mg/kg) and calcein (20 mg/kg) (Meilunbio, China) were administrated intraperitoneally at seven and three days before sacrifice.

X-ray and micro-CT scanning At postoperative 2, 4 and 8 weeks, the femur samples were collected and fixed in 70% alcohol. X-ray imaging was performed at both sagittal and coronal view, and micro-CT scanning was conducted subsequently.

Van-Gieson and Toluidine blue staining After embedded in the PMMA, hard-tissue section was performed via hard tissue slicer [17]. The prepared sections were stained with Van-Gieson (V-G) (Leagene, China) and toluidine blue solution (Solarbio, China). After sealing with neutral gum, observing and photographing were conducted.

SEM and EDS detection The polished sections were pre-treated through spraying gold, and then were observed in SEM. Distribution of elements within the sections were detected using EDS analysis.

Hematoxylin-eosin (HE) staining The critical organs of SD rats including heart, lung, liver, spleen and kidney were stained with HE staining. Briefly, the sections were rehydrated with gradient ethanol, then, stained with hematoxylin (Solarbio, China) for 10min and eosin solution for 1min. Finally, dehydrating with gradient ethanol gradient and sealing with neutral gum. HE staining was also performed for samples from hard tissue sectioning.

2.7. In-vivo antibacterial evaluation

Giemsa staining In-vivo antibacterial performance of the new scaffolds was evaluated via subcutaneous infection model according to previous report, which possessed the advantages of simple operation and relatively short experimental period [18]. Briefly, 6-weeks male C57 mice were randomly divided into four groups. After anesthesia, disinfection and shaving, an 1 cm incision was made in the back skin. The Ta, Ta/Gel and Ta/Gel/PLGA/Van scaffolds were immersed in MRSA with a concentration of 10^7 CFU/mL and implanted subcutaneously, and 200 µL normal saline was injected subcutaneously for liquid exchange after

suturing [18]. 200 μL vancomycin was injected in the positive control group. At 1 week postoperatively, the subcutaneous tissues were collected and fixed using 4% PFA. After slicing, the sections were stained with Giemsa solution (Solarbio, China).

Bacterial counting As for bacterial counting of in-vivo tissue, after the mice were sacrificed, scaffolds and surrounding tissues were collected in centrifugal tubes. PBS were added and bacteria were eluted by dramatical shocking. 100 μL diluted in-vivo bacterial liquid were scribbled on the plates and photographed next day.

2.8. Statistical analysis

All quantitative data were collected in the form of mean \pm standard deviation (mean \pm SD). Independent-samples T-test and one-way analysis of variance (one-way ANOVA) were selected for the data analyses between two groups and over two groups flexibly. A *P* value of 0.05 was set as the threshold of statistically significant difference (*, *P* < 0.05).

3. Results

3.1. Isolation and identification of BMSCs

After chondrogenic differentiation induction for 21 days, regular chondrospheres with a diameter about 1 mm formed, of which the section was stained with light blue by Alcian blue (Fig. S1a). Alizarin red staining showed that considerable orange-red irregular calcium nodules appeared on the surface of BMSCs after osteogenic differentiation induction for 14 days (Fig. S1b). In addition, Oil Red O staining showed that red lipid droplets with various sizes formed after chondrogenic induction (Fig. S1c).

3.2. Influence of different antibiotics on BMSCs proliferation and osteogenesis

In-vitro cellular experiments were carried out to evaluate the influence on BMSCs proliferation and osteogenesis of different antibiotics. The same concentration of vancomycin (500 $\mu\text{g}/\text{mL}$) was used in all the cell experiments, which was much higher than the minimum inhibitory concentration (MIC) for MRSA reported previously (>1 $\mu\text{g}/\text{mL}$). EDU/DAPI fluorescence staining showed that the blue/red fluorescence rate were not significantly different between the Van-treated and control groups, both of which were significantly more than the other two groups, with the least in the Nor-treated group (Fig. S2). As shown in Fig. S3a, from day 3 to day 7, increased ALP clusters were found in the Van-treated and control groups, while no obvious increase was found in the Gen-treated group. On the contrary, ALP clusters in the Nor-treated group reduced. The semi-quantitative analysis (Fig. S3b) indicated the Gen-treated group was not statistically different from the Nor-treated group, which were less than the control and Van-treated groups. Meanwhile, the quantitative analysis of supernatant ALP production (Fig. S3c) was consistent with the result of ALP staining. The results of alizarin red staining (Fig. S3d) showed obvious orange-red calcium nodules in the Van-treated and control groups at day 12, while relatively less nodules in the other two groups. When cultured to day 21, bulks calcium nodules were observed in the Van-treated and control groups, with a little of calcium nodules in the Gen- and Nor-treated groups. Meanwhile, the degraded solutions of calcium nodules in the control and Van-treated groups (Fig. S3e) got darker from the day 12 to day 21, while the Gen- and Nor-treated groups were always lavender. The semi-quantitative analysis of alizarin red staining and OD value of degraded solution were depicted in Fig. S3f and Fig. S3g respectively, both of which were consistent with the previous results. At day 12 and day 21, no significant difference was found in the Van-treated and control group, while reduced calcium nodules was detected in the Gen- and Nor-treated groups. Similarly, the result of Sirius Red staining (Figs. S3h–k) was in line with that of alizarin red staining. The qRT-PCR results of

osteogenesis-related genes (Fig. S4) indicated that expression of osteopontin (*OPN*), osteocalcin (*OCN*) and Runt-related transcription factor 2 (*RUNX2*) genes did not differentiate significantly between the control and Van-treated groups at day 3. Expression of *OPN* and *OCN* in Gen-treated group was significantly higher than Nor-treated group, but lower than the other two groups. However, expression of *RUNX2* was not significantly different between the Nor- and Gen-treated groups (Fig. S4a). At day 7, expression levels of osteogenesis genes in the control and Van-treated groups were significantly higher than the other two groups (Fig. S4b). At day 14, there was no obvious difference regarding expression of *OCN*, *OPN* and *RUNX2* between the control and Van-treated groups, all of which were much higher than the Gen- and Nor-treated groups. And *OCN* expression in the Gen-treated group was significantly higher than the Nor-treated group (Fig. S4c). These results synergistically demonstrated that Gen and Nor suppressed proliferation and osteogenic differentiation of BMSCs, and Van were well biocompatible and showed no obvious effect on the osteogenesis of BMSCs.

3.3. Preparation and characterization of AM-Ta

AM-Ta scaffolds were designed with regular dodecahedron structure (Fig. S5a), and Ta powders, raw materials for additive manufacturing, were black and high-density (Fig. S5b). The SEM characterization (Fig. S5c) showed that Ta powder was densely distributed at low magnification, most of which were irregular and some were spherical. High-magnification view indicated that Ta powder distributed evenly, and some spherical Ta powders clustered together. Porous Ta scaffolds (Fig. S5d) with size of $\Phi 4\text{mm} \times 5\text{ mm}$ and $\Phi 3\text{mm} \times 4\text{ mm}$ were successfully prepared via selective laser melting (SLM) technology. The SEM characterization demonstrated the uniformly-distributed pore structure and uniform pore size on the top of AM-Ta scaffolds (Fig. S5e), and pores interconnected each other. The pore and beam size of AM-Ta scaffolds were about 450 μm and 300 μm respectively. The surface of the porous Ta scaffolds was rough and rugged gully-like microstructure could be also observed, with some incompletely-molten spherical Ta powders remaining on the surface. The EDS results (Fig. S5f) indicated only Ta and oxygen element were found on the surface, confirm the composition of AM-Ta scaffolds.

3.4. Fabrication and characterisation of the composite Ta/Gel/PLGA/van scaffolds

In this study, the double emulsion method was applied to prepare the Van-encapsulated PLGA microspheres. PLGA used to prepare microspheres was white, transparent, and odorless granules (Fig. S6a), which could be dissolved in dichloromethane through sonication (Fig. S5d). Van was gray-white fine powder (Fig. S6b) and became gray and turbid solution when dissolved in ddH₂O (Fig. S6e). PVA was pure white particle (Fig. S6c), which was colorless and transparent when dissolved in ddH₂O after heating (Fig. S6f). When the water-phase Van solution was added into the oil-phase PLGA solution, obvious stratification appeared with vancomycin on the upper and PLGA on the lower (Fig. S6g). Under ultrasonic treatment, the Van/PLGA mixture became homogeneous and stable milky-white emulsion without stratification or precipitation (Fig. S6h). Prepared Van-encapsulated PLGA microspheres were white when dispersed in ddH₂O (Fig. S6i), which were insoluble and gradually sedimented. After freeze drying at $-80\text{ }^\circ\text{C}$, the Van-loaded PLGA microspheres present as loose white powders (Fig. S7a). The SEM observation showed (Fig. S7b) that microspheres were regularly spherical and well-distributed. It was worth noting that there were several discontinuous micropores on the surface of microspheres, which distributed in a honeycomb pattern. For single drug-loaded microsphere, the EDS detection identified carbon (C), oxygen (O), chlorine (Cl) and nitrogen (N) elements on the surface, which was consistent with theoretical analysis (Figs. S7c–d). The particle size of Van-encapsulated microspheres ranged from 0 to 100 μm and dominated at 30–39 μm (Fig. S7f),

and the average size was $34.84 \pm 1.04 \mu\text{m}$. Zeta potential test detected a potential of -5.31 mV for Van, 1.44 mV for PLGA, and -13.1 mV for Van-encapsulated PLGA microspheres (Fig. S7e). Van solutions with various concentrations showed specific peaks at 280 nm in the UV spectrophotometer, and the peak values were closely corrected with the concentrations (Fig. S7g). According to the standard curve, the encapsulation efficiency and drug-loading rate were calculated as $46.66 \pm 3.48\%$ and $16.97 \pm 0.84\%$ respectively (Fig. S7h). The releasing feature of Van adsorbed into the porous Ta scaffolds physically and encapsulated in PLGA microspheres was shown in Fig. S7i. Obvious explosive releasing of Van was observed in the physical absorption group, which reached the platform fast with about 90% Van released at day 3. The releasing of Van was significantly slowed down when loaded in the PLGA microspheres, which reached 71.62% at day 15.

All above results suggested that the Van-encapsulated PLGA microspheres were successfully prepared. Then, the PLGA microspheres were mixed with GelMA hydrogel and loaded into the porous AM-Ta to fabricate the composite Ta/Gel/PLGA/Van scaffolds.

GelMA hydrogel of various concentrations showed different structural strength and ductility. 5% (w%) GelMA hydrogel could not solidify completely as stereoscopic scaffolds after UV irradiation, which still had fluidity. While 7.5% and 10% GelMA hydrogels showed similar appearance, both of which could form columns with elasticity and strength (Fig. 1a). In subsequent experiments, the 7.5% GelMA hydrogel receiving 10 s UV lighting was used for producing scaffold to prevent over-gelation, which would affect the release of incorporated van and its antibiotic activity. In the composite Ta/Gel/PLGA/Van scaffold, Van-encapsulated PLGA microspheres evenly distributed inside the GelMA

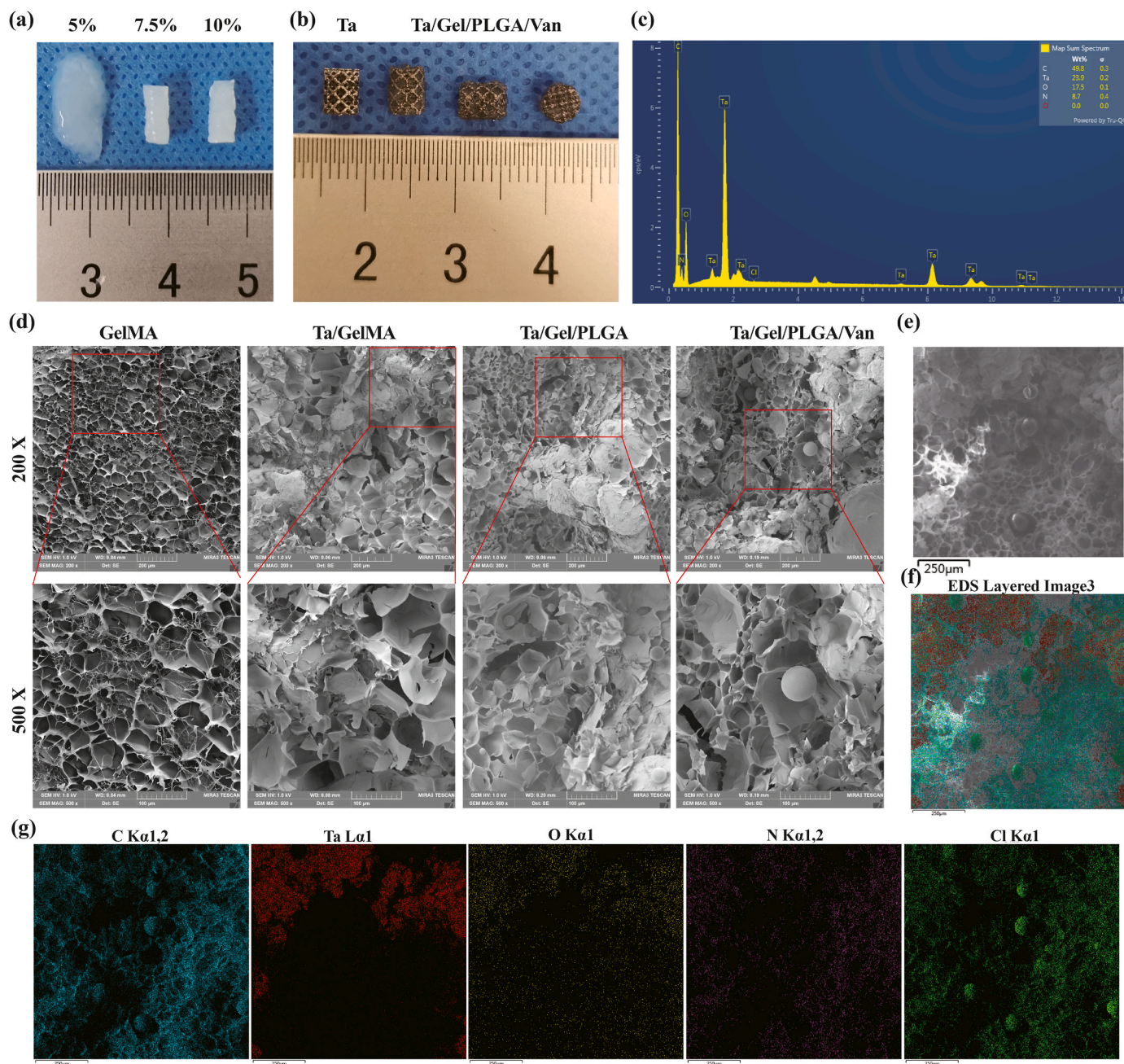


Fig. 1. Fabrication and characterization of the Ta/Gel/PLGA/Van composite scaffolds. (a) General view of 5%, 7.5% and 10% GelMA hydrogels. (b) General view of the Ta/Gel/PLGA/Van composite scaffold. (c) Elements spectrum for the Ta/Gel/PLGA/Van composite scaffolds. (d) Representative SEM image of the novel scaffolds. (e–g) EDS detection of elements distribution.

hydrogel, which filled the pores (Fig. 1b). SEM showed that the surface of GelMA hydrogel was porous and honeycomb, and the pores interconnected with the interior pores (Fig. 1d). The PLGA microspheres were loaded in GelMA hydrogel and distributed evenly, and a small number of PLGA microspheres were found on the beams of the scaffolds. Compared with PLGA microspheres without loading drugs, diameter of Van-loaded PLGA microspheres was larger (Fig. 1d). EDS analysis identified tantalum (Ta), carbon (C), oxygen (O), nitrogen (N) and chlorine (Cl) elements on the surface of the composite scaffolds (Fig. 1c and 1e–g).

These results suggested that the composite Ta/Gel/PLGA/Van scaffolds were successfully fabricated.

3.5. In-vitro antibacterial properties of the Ta/Gel/PLGA/van scaffolds

In-vitro antibacterial tests were performed to evaluate bacteriostatic properties of the Ta/Gel/PLGA/Van scaffolds. The result of the antibacterial ring test was depicted as Fig. 2. There was no bacteriostatic ring around the Ta/Gel scaffolds all the time. At day 1 and day 3, considerable antibacterial rings appeared around the Ta/Van and Ta/Gel/PLGA/Van composite scaffolds, but the bacteriostatic rings around the Ta/Van scaffolds were no longer obvious at day 9 and completely disappeared at day 15. On the contrary, although the diameter of

inhibitive rings around the Ta/Gel/PLGA/Van composite scaffolds also shrank as time going, obvious ring could still be observed at day 15 (Fig. 2a). Corresponding quantitative analysis of the bacteriostatic rings was depicted as Fig. 2b. With respect to the paper disc diffusion method, released solution could also form obvious bacteriostatic rings. Similar with the scaffolds, the inhibitive rings formed by the released solution reduced as time prolonging. From day 3, the Ta/Van group was significantly smaller than the Ta/Gel/PLGA/Van group in terms of diameter of the antibacterial rings, and no rings appeared all the time in the Ta/Gel group (Fig. 2d). The corresponding quantitative analysis of paper disc diffusion method was shown as Fig. 2c. The result of living/dead bacterial staining indicated that a great number of bacteria stained as green could be observed in all groups. Only very few dead bacteria stained as red could be found in the control and Ta/Gel groups. Considerable red bacteria appeared in the Ta/Gel/PLGA/Van and Van-treated groups, and the red fluorescence co-located with green fluorescence (Fig. 2e). As for bacterial counting, numerous spherical MRSA covered the agarose culture plates in the control and Ta/Gel groups, while only several bacteria scattered in the Ta/Gel/PLGA/Van and Van-treated groups (Fig. 2f). Statistical analysis suggested that there was no significant difference regarding bacterial number between the control and Ta/Gel groups, and no significant difference was identified between the Ta/Gel/PLGA/Van and Van-treated groups (Fig. 2g). SEM indicated

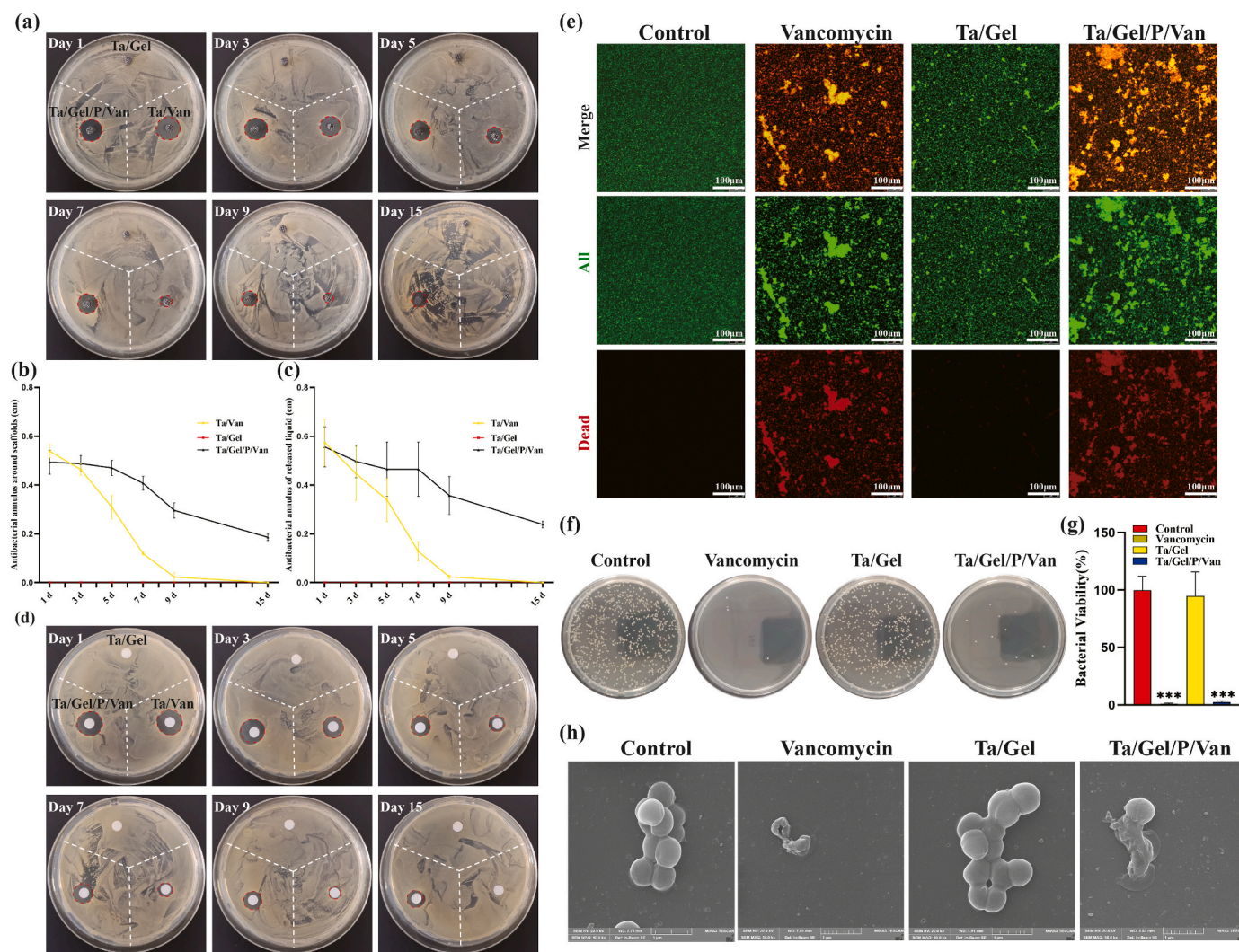


Fig. 2. In-vitro antibacterial activity of the Ta/Gel/PLGA/Van composite scaffolds. (a–b) Antibacterial ring test for scaffolds (a) and corresponding statistical analysis (b). (c–d) Antibacterial ring test for released liquid (d) and corresponding statistical analysis (c). (e) Living/dead bacteria staining. (f–g) Bacterial counting (f) and corresponding statistical analysis (g). (h) Representative SEM images of bacterial morphology after treatment.

that normal MRSA was regularly spherical, and multiple bacteria clustered together. Treated with vancomycin, the MRSA shrank and fell apart. Co-cultured with Ta/Gel scaffold, MRSA gathered into clusters and did not change obviously in terms of shape. After co-cultured with Ta/Gel/PLGA/Van composite scaffolds, MRSA shriveled and ruptured (Fig. 2h).

Above results demonstrated that the newly-developed Ta/Gel/PLGA/Van composite scaffolds introduced in this study possessed potent antibacterial properties *in vitro* and *in vivo*.

3.6. *In-vitro* biocompatibility and osteogenic property of the Ta/Gel/PLGA/van composite scaffold

In order to evaluate the *in-vitro* biological performance of the composite Ta/Gel/PLGA/Van scaffold, cellular adhesion, proliferation and osteogenic differentiation were detected.

EDU/DAPI staining showed that at low magnification, dense blue and red fluorescence signals could be observed in each group. At high magnification, evenly-distributed orange EDU and blue nuclei intersected mutually, and the EDU floated over the nuclei (Fig. S8a). The result of CCK8 was shown as Fig. S8b. At the 1st day, there was no statistical difference in OD values of each group. As time going, OD values gradually increased, which rose to more than 2.0 at the 5th day. And no significant difference was identified among all the groups at different time points. Living/dead cell staining indicated that when co-cultured with the scaffolds, abundant living cells stained as green and very few dead cells stained as red could be observed on the surface of scaffolds (Fig. S8f). Cells distributed along with the surface morphology of the scaffolds. At 3rd day, BMSCs on the surface of scaffolds in each group increased significantly, and living cells in the Ta/Gel and Ta/Gel/PLGA/Van groups covered the scaffolds surface, connecting with each other to form green cellular film. In the Ta/Gel/PLGA/Van group, BMSCs were shaped in long spindle, which were denser and more extended than the Ta group. In some areas, BMSCs grew into the hydrogel and integrated with the scaffold, presenting as three-dimensional structures. The number of living cells on the surface of porous Ta was significantly less than that of other two groups.

The results of nucleus and cytoskeleton staining were shown as Figs. S8c–d. In the two-dimensional view (Fig. S8c), blue nucleus increased and green cytoskeleton extended from day 1 to day 3. At day 1, a small number of blue nuclei surrounded with blurry cytoskeletons appeared on the top of porous Ta scaffold. In the Ta/Gel and Ta/Gel/PLGA/Van groups, blue nuclei and spindle-shaped cytoskeleton evenly distributed on the surface of scaffolds, and the cytoskeletons began to elongate and interleaved with each other. Some cytoskeletons were pale and blurred, indicating the integration between BMSCs and hydrogels. At day 3, obvious blue nuclei surrounded by green cytoskeleton could be observed on the surface of porous Ta. In the Ta/Gel group, cytoskeleton covered about 80% areas, which became typically fusiform. Cytoskeleton of the Ta/Gel/PLGA/Van group was wider and longer than that of the other two groups, with pseudopodia protruding around the cells. Relevant statistical analysis about cytoskeleton/nucleus ratio (CNR) was illustrated as Fig. S8e. At day 1, there was no statistical difference between the Ta/Gel and the Ta/Gel/PLGA/Van groups, both of which were significantly higher than the porous Ta group. At day 3, CNR of the Ta/Gel/PLGA/Van group was significantly higher than that of porous Ta group. The corresponding three-dimensional view was depicted in Fig. S8d. It can be seen that BMSCs did not fully spread out at the 1st day, most of which were spherical and clustered. At the 3rd day, BMSCs on the porous Ta surface extended gradually. In the Ta/Gel and Ta/Gel/PLGA/Van composite groups, BMSCs interlinked to form tridimensional structure, which integrated with the hydrogel of the scaffolds. Fig. S8g showed the adhesion of BMSCs on the surface of the scaffold detected by SEM. At day 1, BMSCs (red arrow) on porous Ta were shaped in short spindle, with a few pseudopodia sticking out and sticking to the beams. In the Ta/Van group, chapped Van (blue arrow) could be observed, and

BMSCs adhered poorly and no cells were found at where Van adsorbed. In the Ta/Gel group, pores of Ta scaffolds were filled with GelMA hydrogel (yellow arrow). Some hydrogel cracked after drying and BMSCs with typical long-spindle shape adhered to the surface. In the Ta/Gel/PLGA/Van group, a large number of BMSCs and Van-loaded PLGA microspheres could be observed on the surface of the scaffolds (purple arrow). At the 3rd day, BMSCs on the surface of the porous Ta scaffold increased significantly, which spread and connected mutually to form cellular film. Only several cells were found in the Ta/Van group, which were atrophic without obvious pseudopodia. BMSCs in the Ta/Gel/PLGA/Van group became more complex and connected to form dense cellular films, covering the surface of the scaffolds.

All of these results indicated that the novel Ta/Gel/PLGA/Van scaffolds were well biocompatible.

ALP is an acknowledged marker of early osteogenesis, which is usually detected using staining and quantification for evaluating inchoate osteogenic differentiation [16]. After cultured with releasing solution for 3 days, light blue ALP could be found in each group, which distributed uniformly with no significant difference among the groups. When cultured for 7 days, the bottom of the wells was completely stained as blue and BMSCs became denser, and ALP color significantly deepened (Fig. 3a). Corresponding statistical analysis showed that production of ALP increased significantly from day 3 to day 7, but there was no significant statistical difference between all the group at two time points (Fig. 3b). Quantifying the ALP production in the supernatant demonstrated that ALP content of the porous Ta group was higher than that of other three groups at day 3 with the control group being the lowest, but no statistical significance was detected at day 7 (Fig. 3c). The results of alizarin red staining were depicted as Fig. 3d. After osteogenic induction for 14 days, a few red mineralized nodules scattered at the bottom of well plates, and the cellular film formed by BMSCs could be seen in some areas. When cultured with releasing solution for 21 days, the bottom of well plates was completely covered with dark-red nodules. Under the microscope, mineralized nodules with different sizes and irregular shapes distributed densely, and interacted with each other to form chunks, with no significant difference among the groups. The solution obtained by degrading the stained mineral nodules was shown as Fig. 3j, which turned from light purple at the 14th to black purple at the 21st day. Corresponding semi-quantitative analyses for alizarin red staining and OD value of degraded solution were depicted as Fig. 3e and f respectively. Both of which indicated that the content of calcium nodules increased significantly as time going, and the difference among the groups was not statistically significant at both time points. Result of Sirius red staining indicated that when BMSCs were cultured with composite scaffold extraction for 12 days, light pink thin film appeared. Type I collagen (COL-1) dots could be observed under microscope, and no obvious difference were found among the groups. At day 21, the bottom of the well plate was completely covered by red film, which deepened significantly in comparison to day 12. As for microscopic view, red COL-1 with irregular shapes and uneven sizes clustered densely (Fig. 3g). The degraded solution was light red for day 12 and dark red for day 21 (Fig. 3k). Semi-quantitative analysis for Sirius red staining detected no obvious difference among the control, Ta, Ta/Gel and Ta/Gel/PLGA/Van groups at different point-in-time (Fig. 3h), and similar result was obtained for the OD values of the degraded solution at 540 nm (Fig. 3i).

When seeding BMSCs on the scaffolds directly, ALP staining showed that cells on the top of scaffolds were stained as light blue at day 3 (Fig. S9a). Especially, blue signal in the porous Ta group distributed on the beams, while signal in the Ta/Gel and Ta/Gel/PLGA/Van groups appeared on the hydrogel. At day 7, the surface of the scaffolds in each group was stained as dark blue, and the hydrogels on the surfaces of Ta/Gel and Ta/Gel/PLGA/Van groups were also deeply-stained with no significant difference among the groups. After 14-days culturing, Sirius red staining showed that the surface of the scaffolds was stained as red. Hydrogel in the Ta/Gel and Ta/Gel/PLGA/Van groups were also stained

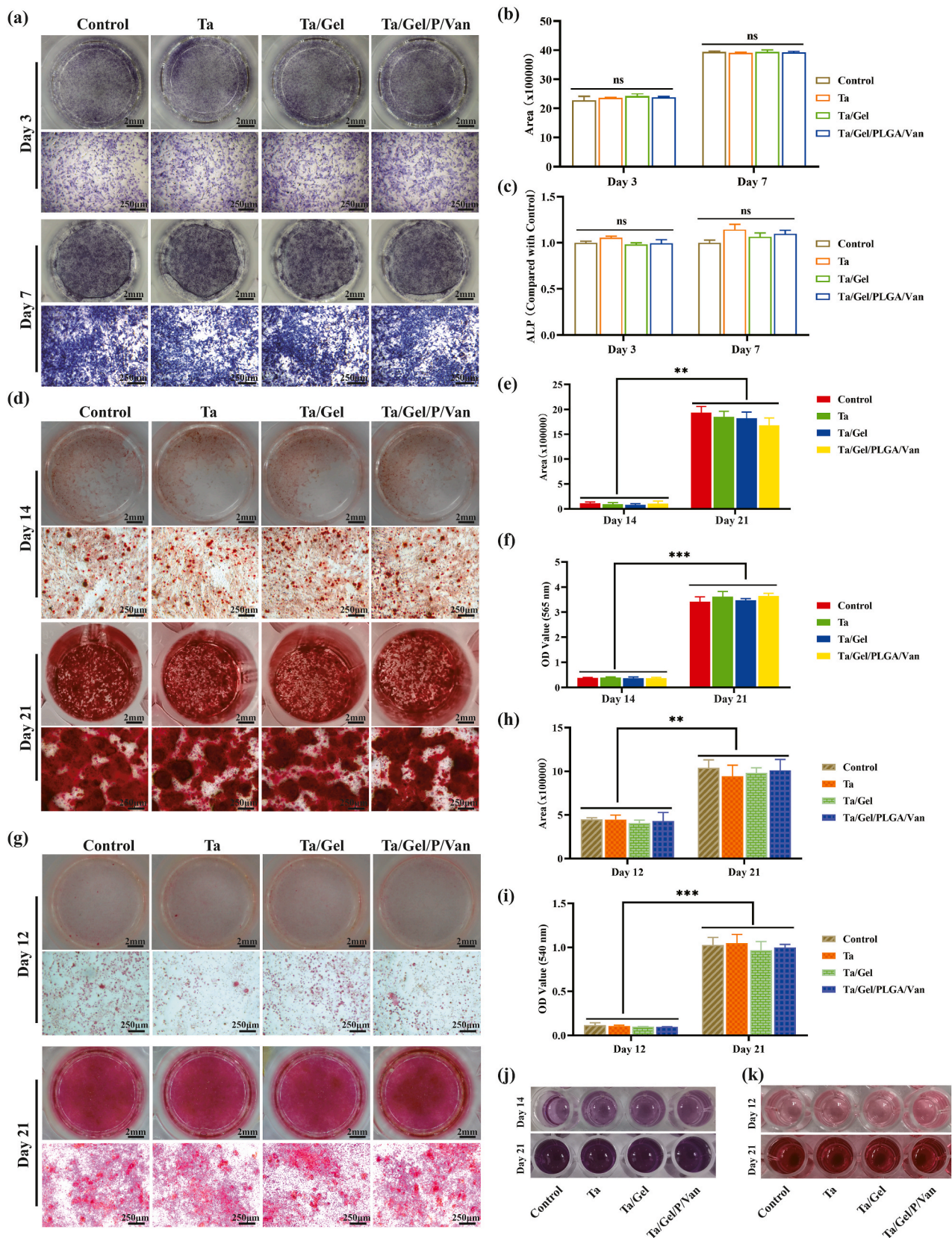


Fig. 3. In-vitro osteogenic properties of the newly-developed composite scaffolds. (a) Alkaline phosphatase (ALP) staining. (b) Semi-quantitative analysis of ALP staining. (c) Detection OF ALP production in the supernatant. (d) Alizarin red staining. (e) Semi-quantitative analysis of alizarin red staining. (j) Degraded solution of alizarin red staining. (f) OD value detection for (j) at 565 nm. (g) Sirius red staining. (i) Semi-quantitative analysis of Sirius red staining. (k) Degraded solution of Sirius red staining. (h) OD value Detection of (k) at 540 nm.

(Fig. S9b). Alizarin red staining indicated that the surfaces of Ta/Gel and Ta/Gel/PLGA/Van groups were stained as dark red, and clustered mineral nodules could be observed on the beams of the porous Ta obviously. In addition, some hydrogel degraded, contributing the deformation of the composite scaffold.

The mRNA expression level of osteogenesis-related genes after cultured with sustained releasing solution of scaffolds for 3 days, 7 days and 14 days was depicted in (Fig. S10). At day 3, expression of *ALP* in the porous Ta group was significantly higher than that of Ta/Gel/PLGA/Van

group, and BMSCs in the Ta group expressed higher *RUNX2* significantly than the other three groups (Fig. S10a). At day 7, expression level of *ALP* in the Ta group was statistically higher than control and Ta/Gel/PLGA/Van groups, and *RUNX2* was expressed significantly higher in the Ta group than the Ta/Gel group (Fig. S10b). At day 14, there was no significant difference in the expression of Bone Morphogenetic Protein 2 (*BMP2*), *OPN*, *RUNX2* and *COL1* among all groups (Fig. S10c). Higher-level *ALP* mRNA was detected in the Ta/Gel group than the control group, and BMSCs in the Ta/Gel group expressed *OCN* more abundantly

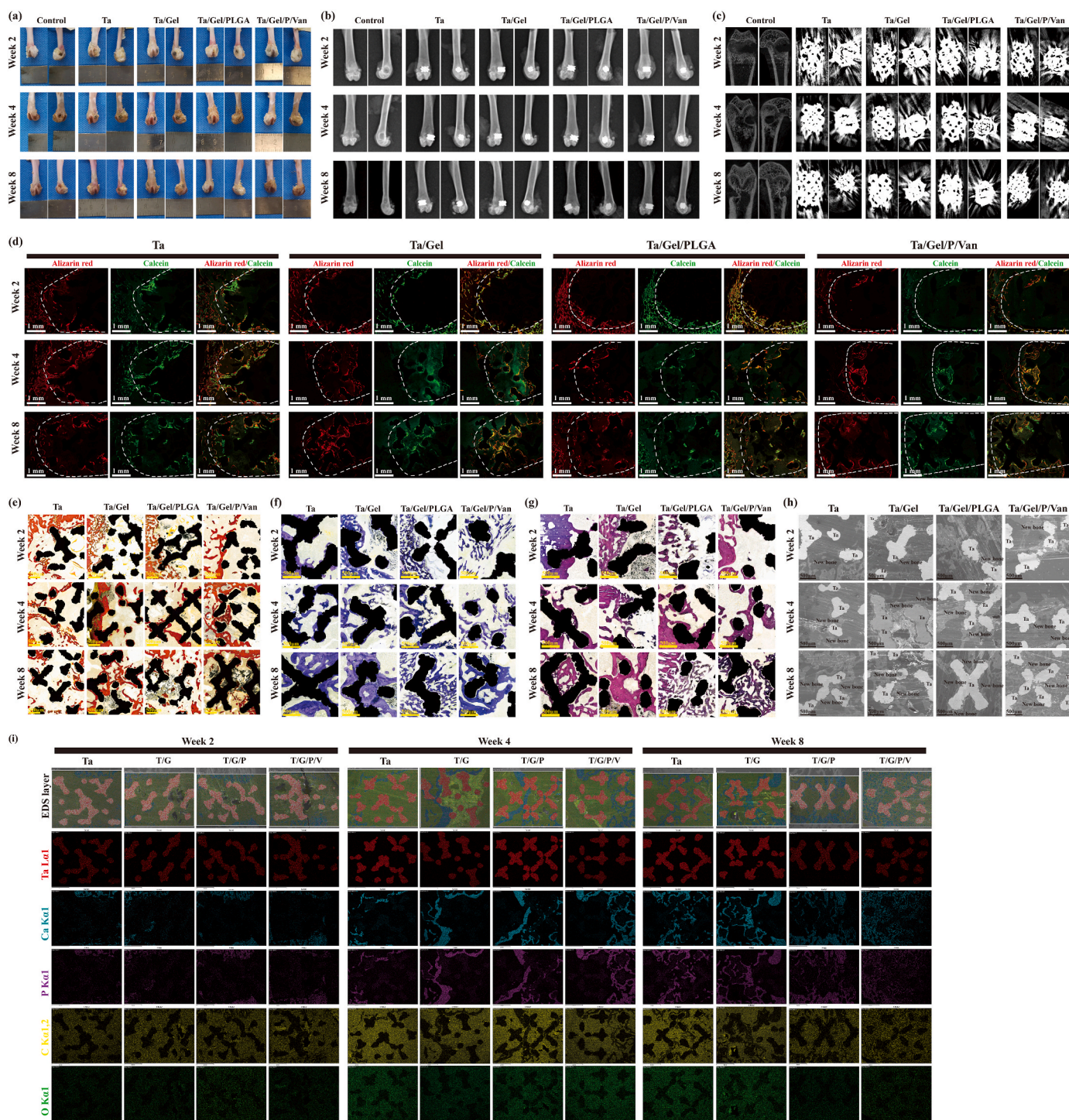


Fig. 4. In-vivo efficiency of the newly-developed scaffolds for repairing bone defects. (a) General view of femur specimens at 2, 4 and 8 weeks. (b) Representative X-ray image. (b) Micro-CT scanning. (d) Fluorescence image of sections labelled with alizarin red (red color) and calcein (green color). (e) V-G staining. (f) Toluidine blue staining. (g) HE staining. (h) SEM observation of the new bone ingrowth inside the scaffolds. (i) EDS detection of elements distribution inside the sections.

than the porous Ta and Ta/Gel/PLGA/Van groups (Fig. S10c). In conclusion, there was no significant difference in mRNA expression among all groups.

3.7. In-vivo performance of the Ta/Gel/PLGA/van scaffolds for repairing bone defect

The fabricated composite scaffolds used for repairing bone defects in vivo was illustrated as Fig. S11a. After implanted into the bone defects, the top of the composite scaffolds was flush with the surface of the bone defect, and the margin of scaffolds was tightly compacted with the edge of bone defects (Fig. S11b). Fig. 4a depicted the general view of the femur specimens after implantation for 2 weeks, 4 weeks and 8 weeks. At the 2nd week, there were obvious cavity at the distal femur of the control group. It could be seen that the scaffolds were perpendicular to the distal femur and closely combined with the bone tissue in all scaffold-implantation groups. At the 4th week, cavity in the control group reduced, and soft tissues covering the scaffolds increased in the Ta-containing groups. At the 8th week, it could be seen that the cavity became smaller than before in the control group, but still existed. No obvious defects were found in other Ta-containing groups. The corresponding X-ray images were shown as Fig. 4b. Even at the longest 8th week postoperatively, there was still obvious voids within the bone defect of the control group, which could not recover by itself. As expected, cylindrical scaffolds were fixed in the distal femur, perpendicular to the femoral shaft, with no obvious loosening and detachment observed at different time points among all groups. The thin gaps between the scaffolds and the host bone reduced gradually and disappeared as time prolonging. The micro-CT scanning was illustrated as Fig. 4c. In the control group, a cylindrical defect could be seen clearly at the distal femur. In the Ta-containing groups, the scaffolds appeared as rectangular in the sagittal view, and round in the coronal view. Obvious radial metallic artifacts scattered around the scaffolds, which covered the newly-formed bone. It's a pity that quantitative analysis could not be performed due to the presence of metal artifacts.

Fluorescence labelling indicated that there was considerable bone ingrowth within the scaffolds, and the bone formation increased gradually as time going (Fig. 4d). Host bones were labelled by alizarin red, which appeared as red signal in the confocal microscopy. Newly-regenerated bones were labelled by calcein, which appeared as green signal. At 2 weeks, a small amount of red and green fluorescence could be seen around the defect edge, and the fluorescence surrounded the scaffolds beams closely. The fluorescence signal in the Ta/Gel/PLGA/Van group was less than the other three groups. At 4 weeks, the fluorescence distribution areas within the scaffolds increased significantly in each group. At 8 weeks, the fluorescence extended to filled most area of the defects, indicating the well integration between the implanted scaffolds and the host bone, and there was no significant difference among the groups. In V-G staining images, Ta metal appeared as black, while bone tissue was marked as red (Fig. 4e). At the first time point, bone tissue attached onto the beams of the scaffolds, and a small amount of red new bone tissue grew into the scaffolds within limited depth and area. At the 4th week, more red new bone grew inside the scaffolds in each group, and the ingrown depth increased. New bone surrounded the scaffolds to integrate together, and no obvious cracks were observed between the new bone and the Ta metal. At week 8, new bone distributed throughout the whole scaffold, and some beams of the scaffolds were circumvolved by newly-regenerated bone tissue. A few gray clusters were observed in Ta/Gel, Ta/Gel/PLGA and Ta/Gel/PLGA/Van groups. The results of toluidine blue staining were consistent with V-G staining (Fig. 4f). At 2 weeks, a small amount of bone tissue stained as bluish violet appeared around the Ta scaffolds, wrapping the edge closely. As time went on, the bone tissue gradually grew inside the scaffolds, beginning to wrap the scaffolds. And finally, the new bone tissue integrated with the scaffolds closely. HE staining results was illustrated as Fig. 4g, in which Ta metal showed as black and bone tissue

was marked as purplish red. Similar with above V-G and toluidine blue staining, at first, new bone tissue surrounded the margin of the scaffolds, and the bone ingrowth increased as time going, which finally wrapped and integrated with the scaffolds closely. SEM detection of hard tissue sections showed that Ta metal appeared as silvery white, while new bone tissue looked gray (Fig. 4h). With time extending, gray bone tissue increased gradually and covered the cross-sectional view at 8 weeks finally. EDS analysis was performed (Fig. 4i). Different elements were marked as various colors, red for Ta, cyan for calcium (Ca), purple for phosphorus (P), yellow for carbon (C), and green for oxygen (O). Visible blue and purple signals could be found in where red signal was absent, suggesting that the new bone grew into the scaffolds. And it could be seen that from 2 weeks to 8 weeks, cyan and purple signals gradually increased and filled the areas where there was no red signal.

3.8. In-vivo biocompatibility of the Ta/Gel/PLGA/van scaffolds

Blood routine examination result was illustrated as Fig. S12. After implantation for 2 weeks, no obvious difference was identified among the groups (Fig. S12a). At 4 weeks, the lymphocytes percentage of Ta group were significantly lower than that of Ta/Gel/PLGA/Van group, while Ta group was significantly higher than Ta/Gel/PLGA/Van regarding the granulocyte percentage (Fig. S12b). At 8 weeks, monocytes of the Ta/Gel/PLGA/Van group were significantly higher than the other four groups (Fig. S12c). Detection for the liver and kidney function indexes at postoperative 2, 4 and 8 weeks was shown as Fig. S13. There was no statistical difference was detected among all the groups at 2 weeks after implantation (Fig. S13a). At 4 weeks, aspartate transaminase (AST) of the Ta/Gel/PLGA and Ta/Gel/PLGA/Van groups were significantly higher than the other groups. Meanwhile, the Ta/Gel/PLGA and Ta/Gel/PLGA/Van groups were significantly higher than the control group in terms of uric acid (UA) (Fig. S13b). At 8 weeks, blood urea nitrogen (BUN) of the control group was significantly higher than the other four groups (Fig. S13c). HE staining for the sections of critical organs including heart, liver, spleen, lung and kidney at 2, 4 and 8 weeks postoperatively were illustrated in Fig. S14a, Fig. S14b and Fig. S14c respectively. Cardiac sections showed fusiform myocardial fibers with clear texture. In liver sections, liver lobule, central vein could be observed, and liver cells radially arranged around the central vein. Blue nodules formed by aggregated cells could be seen in spleen sections. There were lung vacuoles and a small number of blue neutrophils in the lung sections. Kidney sections showed that there were uniformly-distributed glomerulus. There was no significant difference among the control group and other scaffolds-implantation groups.

3.9. In-vivo antibacterial performance of the Ta/Gel/PLGA/van scaffolds

The result of Giemsa staining was depicted as Fig. S15a. After implantation for 1 weeks, massive MRSA stained as orange could be observed around the subcutaneous tissue in the control and Ta/Gel groups. However, only several bacteria remained in the Van-treated and Ta/Gel/PLGA/Van groups, and quantitative analysis was shown as Fig. S15c. Bacterial-counting experiment indicated that almost no bacteria remained the Van-treated group. There was no significant difference between the control and Ta/Gel groups, in both of which a great number of bacteria were eluted from the subcutaneous tissue and scaffold. In addition, compared with the control and Ta/Gel groups, bacterial number of the Ta/Gel/PLGA/Van group was significantly reduced (Fig. S15b). Fig. S15d showed the result of statistical analysis for bacterial counting test.

4. Discussion

The main difficulty of IBDs treatment lies in the structural reconstruction of bone defects and infection elimination, which requires not only the matched geometric structure and mechanical support, but also

the removal of the localized pathogenic bacteria and restoration of the osteogenic microenvironment simultaneously [19,20].

To repair bone defects, autologous bone transplantation has been the "gold standard", followed by allograft and other biomaterial implantation [21]. However, autologous cancellous bone transplantation was denounced by "donor disease" and limited resource [22]. Allogeneic bone transplantation has the risk of disease transmission and rejection [22]. For synthetic materials, both bioceramics and polymers were too poor in strength to provide mechanical support immediately [23]. Porous metals had a wide range of sources and adjustable mechanical properties. In particular, the porous structure could decrease the elastic modulus, thereby reducing the "stress shielding" effect [24]. Currently, Titanium (Ti) and its alloys are the most widely used metals in orthopaedic practice [25]. However, due to its biological inertia, Ti showed poor osteointegration properties, and its alloy was reported to release toxic elements such as aluminum and vanadium, causing biological toxicity [24,26]. In recent years, a great number of laboratory studies and clinical trials have proved that Ta possesses good biocompatibility and specific osteogenic properties [27]. It is well known that geometry and mechanical properties matched with natural bone tissue were beneficial for the integration between implants and the host bone tissue [9,28,29]. Therefore, additive manufacturing technology showed unique advantages in producing orthopedic implants, since it allows for free design and personalized customization of orthopaedic implants.

Clinically, the main pathogenic bacteria accounting for IBDs were gram-positive bacteria, including *Staphylococci*, *Enterococci* and *Streptococcus*, among which *Staphylococci* was the most common [19,30]. Aminoglycoside, quinolone and glycopeptide antibiotics had a wide antibacterial spectrum and were commonly used in the clinical treatment of IBDs. Although their antibacterial efficiency has been verified in clinical practice, their biological effect on normal BMSCs was rarely reported. Previous studies found that different antibiotics showed different effects on cellular proliferation and osteogenic differentiation [31]. In this study, we found that Van had better biocompatibility with BMSCs than Gen and Nor, and showed no significant influence on osteogenic differentiation, making it more suitable as an antibacterial agent for composite scaffolds.

To our best knowledge, there were few reports about loading antibiotics using porous AM-Ta. Sautet, P et al. loaded Van onto modular porous Ta through the simple immersing method and evaluated the elution kinetics, finding that Van was burst released and the drug concentration was as high as 3172 µg/ml in the first hour, with the releasing duration less than 5 days [32]. Rodríguez-Contreras, A et al. used polyhydroxyalkanoates (PHAs) to coat Gen on the modular porous Ta, but the releasing feature and biological properties were not reported [33]. Therefore, it remains a challenge how to realize the long-acting sustained releasing of antibacterial drugs and avoid its biotoxicity caused by burst-releasing.

Delivering drugs to the targeting location through PLGA microspheres for sustained releasing was able to improve drug utilization, prolonging the therapeutic effective and reducing systemic toxicity [11, 34]. Therefore, PLGA microspheres were selected as the first carrier of vancomycin in this study. The particle size of PLGA microspheres was closely associated with the properties, and significantly affected the encapsulation efficiency, drug-loading rate and in vitro releasing feature. According to previous literatures, microspheres with a particle size larger than 20µm was beneficial for sustained releasing [35]. The particle size of PLGA microspheres was influenced by many factors, including PLGA concentration, stirring speed, injection speed, etc. [36, 37]. Previous study reported that the faster the stirring speed was, the smaller the particle size would be [37]. The encapsulation and drug loading rates in this study were $46.66 \pm 3.48\%$ and $16.97 \pm 0.84\%$ respectively, which were consistent with previous reports [37].

Potent antibacterial property was necessary for ideal scaffolds for repairing IBDs. In order to evaluate the antibacterial activity of the scaffolds introduced in this study, MRSA ATCC-43300 was selected for

testing, and results demonstrated the excellent in-vitro/vivo antibacterial performance. Studies suggested that the overuse of antibiotics was the main reason for the emergence of drug-resistant bacteria, which usually impeded the efficiency of antibiotics. Additionally, bacteria could quickly adjust the metabolic systems to resist newly-developed antibiotics [38]. Bacteria attached to the surface of implants and colonized in the form of biofilms. Biofilms were complex composing of bacteria and its secreted extracellular polymeric substances (EPS), which were related to the infection recurrence directly [39]. Biofilms helped the bacteria escape from drug attack through multiple approaches. Firstly, biofilms formed an impenetrable physical barrier which prevented the diffusion of antibiotics, phagocytosis of macrophages, and attack of reactive oxygen species (ROS). Therefore, when removing bacteria encapsulated in biofilms, local antimicrobial drugs needed to reach the minimum biofilm eradication concentration (MBEC), which was much higher than the minimum drug concentration for planktonic bacteria [40]. Secondly, bacteria within biofilms were particular in pathogenic due to the phenotypic diversity, which made them highly resistant to antibiotics [41].

Bone formation was a complex and orchestrated process, including cellular adhesion, proliferation, and deposition of extracellular mineralized matrix, among which BMSCs proliferation is the basis [42]. Scaffolds for repairing IBDs at one stage should possess both well biocompatibility and osteointegration properties. In this study, all materials and metal substrate applied for fabricating the composite scaffold have been recognized as biocompatible. BMSCs were co-cultured with the newly-developed scaffolds, and the biocompatibility was evaluated using CCK8, EDU/DAPI staining, living/dead cell staining, cytoskeleton staining and SEM characterization. ALP staining, alizarin red staining, Sirius red staining and qRT-PCR were performed to evaluate the osteogenic properties. These cell experiments indicated well biocompatibility and in vitro osteogenesis properties of the composite scaffold. As time going, the GelMA hydrogel degraded and the porous structure of the composite scaffolds appeared gradually, which provided suitable environment for bony ingrowth and osteointegration. This special "Antibacteria-Degradation-Bone ingrowth" process is adverse for the biofilm's formation but beneficial for the ingrowth of new bone tissue into porous scaffolds. In-vivo bone integration was a dynamic process regulated by multiple mechanisms, which is much more complex than in vitro [43]. The concentration of vancomycin released from the scaffolds has an acceptable antibacterial effect, and the sustained release behavior of vancomycin from PLGA nanoparticles lasted more than 2 weeks. Despite the absence of the concentration information of Van in scaffolds, these experimental results consistently demonstrated a higher vancomycin concentration > MIC over 2 weeks. In order to further explore the biological safety and property for repairing bone defects, a model of distal-femur bone defect, which was a classic model to detect the osseointegration performance of scaffolds, was established in SD rats to demonstrate the considerable osteointegration performance of the composite scaffold. Although the mechanical properties were not tested in this study, the combination between sustained-release system and porous Ta involved little changes in the physicochemical properties of porous Ta, which was roughly consistent to our previous study [44]. For the treatment of IBDs, currently-designed scaffolds not only concentrated on structural filling and bacterial eradication, but also on enhance of osteogenic activity via loading bioactive agents [7,45]. It was also reported that antibacterial and osteogenic activities could be obtained through single material simultaneously [46,47]. The present study focused on structural reconstruction and bacterial elimination in the infectious fields, without applying additional bioactive agents to improve osteogenesis, since the Ta had specific osteogenesis properties. And also, more related work using susceptible animal models would further demonstrate the antibacterial properties of the composite scaffold explored in this study.

In brief summary, focusing on IBDs, we fabricated and characterized the novel composite scaffolds, and evaluated its biological performance

in vitro and vivo. The Ta/Gel/PLGA/Van scaffolds developed in this study were innovative and practical. While we must acknowledge that some drawbacks remained in this study. Firstly, the scaffolds were not evaluated using the IBDs animal model although subcutaneous infection model and distal-femur defect were applied. Secondly, the biomechanical tests were not performed to explore the in-vivo osteointegration strength. More efforts need to be made for the perfection and clinical application of this novel scaffold.

5. Conclusion

In summary, in the present study, a novel Ta/Gel/PLGA/Van scaffold was fabricated for repairment of IBDs through double emulsion method and ultraviolet gelation. AM-Ta could reconstruct the bone defects structurally and the released Van eliminated the bacteria simultaneously. The results suggested that the newly-developed scaffolds possessed considerable bacteriostatic performance, biocompatibility and osteointegration property, indicating the potent potential for clinical translation and application.

Ethics approval and consent to participate

This animal experiment was approved by the Ethics Committee of Central South University, and all procedures were conducted in accordance with relevant experimental specifications strictly. The ethics approval number is 2021sydw0113.

CRedit authorship contribution statement

Hu Qian: Investigation, Visualization, Writing – original draft, Investigation, Visualization, Writing – original draft. **Ting Lei:** Investigation, Visualization, Writing – original draft. **Long Hua:** Visualization, Investigation. **Yu Zhang:** Data curation. **Dongyu Wang:** Investigation. **Jiangyu Nan:** Methodology. **Wenbin Liu:** Methodology. **Yan Sun:** Software, Validation. **Yihe Hu:** Conceptualization, Supervision. **Pengfei Lei:** Conceptualization, Supervision.

Declaration of competing interest

The authors declare that they have no known competing financial interests or personal relationships that could have appeared to influence the work reported in this paper.

Acknowledgments

This study was supported by the Key research and development program of Hunan Province (Grant No. 2020SK2008 and 2021GK2012), the Major science and technology projects of Changsha City (Grant No. kh2003016). Clinical research fund of National Clinical Research Center for Geriatric Disorders (Xiangya Hospital, Grant No. 2020LNJJ15). The Natural Science Foundation Exploration Project of Zhejiang Province, China (Grant No. Y23H060040), the Natural Science Foundation of Hunan Province, China (Grant No. 2022JJ30934).

Appendix A. Supplementary data

Supplementary data to this article can be found online at <https://doi.org/10.1016/j.bioactmat.2022.12.013>.

References

- [1] S. Wei, J.X. Ma, L. Xu, X.S. Gu, X.L. Ma, Biodegradable materials for bone defect repair, *Mil Med Res* 7 (2020) 54.
- [2] T. Cheng, H. Qu, G. Zhang, X. Zhang, Osteogenic and antibacterial properties of vancomycin-laden mesoporous bioglass/PLGA composite scaffolds for bone regeneration in infected bone defects, *Artif. Cell Nanomed. Biotechnol.* 46 (2018) 1935–1947.

- [3] H. Wang, X.Q. He, T. Jin, Y. Li, X.Y. Fan, Y. Wang, Y.Q. Xu, Wnt11 plays an important role in the osteogenesis of human mesenchymal stem cells in a PHA/FN/ALG composite scaffold: possible treatment for infected bone defect, *Stem Cell Res. Ther.* 7 (2016) 18.
- [4] H. van de Belt, D. Neut, W. Schenk, J.R. van Horn, H.C. van der Mei, H.J. Busscher, Infection of orthopedic implants and the use of antibiotic-loaded bone cements. A review, *Acta Orthop. Scand.* 72 (2001) 557–571.
- [5] T.A.G. van Vugt, J.J. Arts, J.A.P. Geurts, Antibiotic-loaded polymethylmethacrylate beads and spacers in treatment of orthopedic infections and the role of biofilm formation, *Front. Microbiol.* 10 (2019) 1626.
- [6] H. Tan, S. Guo, S. Yang, X. Xu, T. Tang, Physical characterization and osteogenic activity of the quaternized chitosan-loaded PMMA bone cement, *Acta Biomater.* 8 (2012) 2166–2174.
- [7] H. Lu, Y. Liu, J. Guo, H. Wu, J. Wang, G. Wu, Biomaterials with antibacterial and osteoinductive properties to repair infected bone defects, *Int. J. Mol. Sci.* 17 (2016) 334.
- [8] B.R. Levine, S. Sporer, R.A. Poggie, C.J. Della Valle, J.J. Jacobs, Experimental and clinical performance of porous tantalum in orthopedic surgery, *Biomaterials* 27 (2006) 4671–4681.
- [9] R. Wauthle, J. van der Stok, S. Amin Yavari, J. Van Humbeeck, J.P. Kruth, A. A. Zadpoor, H. Weinans, M. Mulier, J. Schrooten, Additively manufactured porous tantalum implants, *Acta Biomater.* 14 (2015) 217–225.
- [10] V.K. Balla, S. Banerjee, S. Bose, A. Bandyopadhyay, Direct laser processing of a tantalum coating on titanium for bone replacement structures, *Acta Biomater.* 6 (2010) 2329–2334.
- [11] Y. Su, B. Zhang, R. Sun, W. Liu, Q. Zhu, X. Zhang, R. Wang, C. Chen, PLGA-based biodegradable microspheres in drug delivery: recent advances in research and application, *Drug Deliv.* 28 (2021) 1397–1418.
- [12] K. Yue, G. Trujillo-de Santiago, M.M. Alvarez, A. Tamayol, N. Annabi, A. Khademhosseini, Synthesis, properties, and biomedical applications of gelatin methacryloyl (GelMA) hydrogels, *Biomaterials* 73 (2015) 254–271.
- [13] L. Ma, X. Wang, Y. Zhou, X. Ji, S. Cheng, D. Bian, L. Fan, L. Zhou, C. Ning, Y. Zhang, Biomimetic Ti-6Al-4V alloy/gelatin methacrylate hybrid scaffold with enhanced osteogenic and angiogenic capabilities for large bone defect restoration, *Bioact. Mater.* 6 (2021) 3437–3448.
- [14] N. Celikkin, S. Mastrogiacomo, J. Jaroszewicz, X.F. Walboomers, W. Swieszkowski, Gelatin methacrylate scaffold for bone tissue engineering: the influence of polymer concentration, *J. Biomed. Mater. Res. A* 106 (2018) 201–209.
- [15] J. Fang, X. Zhao, S. Li, X. Xing, H. Wang, P. Lazarovici, W. Zheng, Protective mechanism of artemisinin on rat bone marrow-derived mesenchymal stem cells against apoptosis induced by hydrogen peroxide via activation of c-Raf-Erk1/2-p90 (rsk)-CREB pathway, *Stem Cell Res. Ther.* 10 (2019) 312.
- [16] P. Lei, H. Qian, T. Zhang, T. Lei, Y. Hu, C. Chen, K. Zhou, Porous tantalum structure integrated on Ti6Al4V base by Laser Powder Bed Fusion for enhanced bony-ingrowth implants: in vitro and in vivo validation, *Bioact. Mater.* 7 (2022) 3–13.
- [17] T. Lei, H. Qian, P. Lei, Y. Hu, The increased oxygen content in tantalum leads to decreased bioactivity and osteogenic ability of tantalum implants, *Biomater. Sci.* 9 (2021) 1409–1420.
- [18] H. Liao, X. Miao, J. Ye, T. Wu, Z. Deng, C. Li, J. Jia, X. Cheng, X. Wang, Falling leaves inspired ZnO nanorods-nanoslices hierarchical structure for implant surface modification with two stage releasing features, *ACS Appl. Mater. Interfaces* 9 (2017) 13009–13015.
- [19] Z.Y. Chen, S. Gao, Y.W. Zhang, R.B. Zhou, F. Zhou, Antibacterial biomaterials in bone tissue engineering, *J. Mater. Chem. B* 9 (2021) 2594–2612.
- [20] H.Y. Ahmadabadi, K. Yu, J.N. Kizhakkedathu, Surface modification approaches for prevention of implant associated infections, *Colloids Surf. B Biointerfaces* 193 (2020), 111116.
- [21] A. Ho-Shui-Ling, J. Bolander, L.E. Rustom, A.W. Johnson, F.P. Luyten, C. Picart, Bone regeneration strategies: engineered scaffolds, bioactive molecules and stem cells current stage and future perspectives, *Biomaterials* 180 (2018) 143–162.
- [22] R. Dimitriou, G.I. Mataliotakis, A.G. Angoules, N.K. Kanakaris, P.V. Giannoudis, Complications following autologous bone graft harvesting from the iliac crest and using the RIA: a systematic review, *Injury* 42 (Suppl 2) (2011) S3–S15.
- [23] D. Tang, R.S. Tare, L.Y. Yang, D.F. Williams, K.L. Ou, R.O. Oreffo, Biofabrication of bone tissue: approaches, challenges and translation for bone regeneration, *Biomaterials* 83 (2016) 363–382.
- [24] X. Wang, S. Xu, S. Zhou, W. Xu, M. Leary, P. Choong, M. Qian, M. Brandt, Y.M. Xie, Topological design and additive manufacturing of porous metals for bone scaffolds and orthopaedic implants: a review, *Biomaterials* 83 (2016) 127–141.
- [25] X. Pei, L. Wu, C. Zhou, H. Fan, M. Gou, Z. Li, B. Zhang, H. Lei, H. Sun, J. Liang, et al., 3D printed titanium scaffolds with homogeneous diamond-like structures mimicking that of the osteocyte microenvironment and its bone regeneration study, *Biofabrication* 13 (2020).
- [26] D.D. Bosshardt, V. Chappuis, D. Buser, Osseointegration of titanium, titanium alloy and zirconia dental implants: current knowledge and open questions, *Periodontol* 73 (2000 2017) 22–40.
- [27] G. Huang, S.T. Pan, J.X. Qiu, The clinical application of porous tantalum and its new development for bone tissue engineering, *Materials* (2021) 14.
- [28] H. Lei, T. Yi, H. Fan, X. Pei, L. Wu, F. Xing, M. Li, L. Liu, C. Zhou, Y. Fan, X. Zhang, Customized additive manufacturing of porous Ti6Al4V scaffold with micro-topological structures to regulate cell behavior in bone tissue engineering, *Mater Sci Eng C Mater Biol Appl* 120 (2021), 111789.
- [29] X. Pei, L. Wu, H. Lei, C. Zhou, H. Fan, Z. Li, B. Zhang, H. Sun, X. Gui, Q. Jiang, et al., Fabrication of customized Ti6Al4V heterogeneous scaffolds with selective laser melting: optimization of the architecture for orthopedic implant applications, *Acta Biomater.* 126 (2021) 485–495.

- [30] C.R. Arciola, D. Campoccia, L. Montanaro, Implant infections: adhesion, biofilm formation and immune evasion, *Nat. Rev. Microbiol.* 16 (2018) 397–409.
- [31] C.R. Rathbone, J.D. Cross, K.V. Brown, C.K. Murray, J.C. Wenke, Effect of various concentrations of antibiotics on osteogenic cell viability and activity, *J. Orthop. Res.* 29 (2011) 1070–1074.
- [32] P. Sautet, T. Mékideche, R. Guilhaumou, M.P. Abdel, J.N. Argenson, S. Parratte, M. Ollivier, Vancomycin elution kinetics from porous tantalum metal, *J. Orthop. Res.* 37 (2019) 308–312.
- [33] A. Rodríguez-Contreras, J. Guillem-Martí, O. Lopez, J.M. Manero, E. Ruperez, Antimicrobial PHAs coatings for solid and porous tantalum implants, *Colloids Surf. B Biointerfaces* 182 (2019), 110317.
- [34] D. Ding, Q. Zhu, Recent advances of PLGA micro/nanoparticles for the delivery of biomacromolecular therapeutics, *Mater Sci Eng C Mater Biol Appl* 92 (2018) 1041–1060.
- [35] J.S. Choi, J. Cao, M. Naeem, J. Noh, N. Hasan, H.K. Choi, J.W. Yoo, Size-controlled biodegradable nanoparticles: preparation and size-dependent cellular uptake and tumor cell growth inhibition, *Colloids Surf. B Biointerfaces* 122 (2014) 545–551.
- [36] Z. Zhou, Q. Yao, L. Li, X. Zhang, B. Wei, L. Yuan, L. Wang, Antimicrobial activity of 3D-printed poly(ϵ -Caprolactone) (PCL) composite scaffolds presenting vancomycin-loaded polylactic acid-glycolic acid (PLGA) microspheres, *Med Sci Monit* 24 (2018) 6934–6945.
- [37] X. Qiu, S. Li, X. Li, Y. Xiao, S. Li, Q. Fen, X. Kang, P. Zhen, Experimental study of β -TCP scaffold loaded with VAN/PLGA microspheres in the treatment of infectious bone defects, *Colloids Surf. B Biointerfaces* 213 (2022), 112424.
- [38] A.P. Magiorakos, A. Srinivasan, R.B. Carey, Y. Carmeli, M.E. Falagas, C.G. Giske, S. Harbarth, J.F. Hindler, G. Kahlmeter, B. Olsson-Liljequist, et al., Multidrug-resistant, extensively drug-resistant and pandrug-resistant bacteria: an international expert proposal for interim standard definitions for acquired resistance, *Clin. Microbiol. Infect.* 18 (2012) 268–281.
- [39] W. Weng, X. Li, W. Nie, H. Liu, S. Liu, J. Huang, Q. Zhou, J. He, J. Su, Z. Dong, D. Wang, One-step preparation of an AgNP-nHA@RGO three-dimensional porous scaffold and its application in infected bone defect treatment, *Int. J. Nanomed.* 15 (2020) 5027–5042.
- [40] D.D. Tassew, A.F. Mechesso, N.H. Park, J.B. Song, J.W. Shur, S.C. Park, Biofilm formation and determination of minimum biofilm eradication concentration of antibiotics in *Mycoplasma hyopneumoniae*, *J. Vet. Med. Sci.* 79 (2017) 1716–1720.
- [41] M. Vallet-Regí, D. Lozano, B. González, I. Izquierdo-Barba, Biomaterials against bone infection, *Adv Healthc Mater* 9 (2020), e2000310.
- [42] M.J. Dalby, N. Gadegaard, R. Tare, A. Andar, M.O. Riehle, P. Herzyk, C. D. Wilkinson, R.O. Oreffo, The control of human mesenchymal cell differentiation using nanoscale symmetry and disorder, *Nat. Mater.* 6 (2007) 997–1003.
- [43] H.D. Kim, S. Amirthalingam, S.L. Kim, S.S. Lee, J. Rangesamy, N.S. Hwang, Biomimetic materials and fabrication approaches for bone tissue engineering, *Adv Healthc Mater* 6 (2017).
- [44] L. Hua, H. Qian, T. Lei, W. Liu, X. He, Y. Hu, P. Lei, Triggering drug release and thermal-disrupting interface induced mitigation of composite photothermal hydrogel treating infectious wounds, *Front. Bioeng. Biotechnol.* 9 (2021), 796602.
- [45] D. Wang, Y. Liu, Y. Liu, L. Yan, S.A.J. Zaafar, D. Wismeijer, J.L. Pathak, G. Wu, A dual functional bone-defect-filling material with sequential antibacterial and osteoinductive properties for infected bone defect repair, *J. Biomed. Mater. Res. A* 107 (2019) 2360–2370.
- [46] X. Shen, Y. Zhang, P. Ma, L. Sutrisno, Z. Luo, Y. Hu, Y. Yu, B. Tao, C. Li, K. Cai, Fabrication of magnesium/zinc-metal organic framework on titanium implants to inhibit bacterial infection and promote bone regeneration, *Biomaterials* 212 (2019) 1–16.
- [47] K. Huo, X. Zhang, H. Wang, L. Zhao, X. Liu, P.K. Chu, Osteogenic activity and antibacterial effects on titanium surfaces modified with Zn-incorporated nanotube arrays, *Biomaterials* 34 (2013) 3467–3478.